Trap-limited diffusion of Zn in β-Ga$_2$O$_3$

Ylva K. Hommedal , Ymir K. Frodason , Lasse Vines , and Klaus Magnus H. Johansen

Department of Physics, Centre for Material Science and Nanotechnology, University of Oslo, P.O. Box 1048, Blindern, Oslo N-0316, Norway

Diffusion of Zn in (001)- and ($\bar{2}$01)-oriented β-Ga$_2$O$_3$ was studied using secondary-ion mass spectrometry and first-principles calculations based on hybrid and semilocal functionals. The β-Ga$_2$O$_3$ samples were sealed in quartz ampules together with a piece of metallic Zn and heated to temperatures of 900–1100 °C for 1 h. The Zn concentration profiles as a function of depth were simulated by employing the trap-limited diffusion model. From this model the migration barrier for Zn diffusion was found to be $E_m = 2.2 \pm 0.2$ and 2.1 ± 0.1 eV in the (001) and ($\bar{2}$01) orientations of β-Ga$_2$O$_3$, respectively, with corresponding dissociation energies of $E_d = 3.5 \pm 1.1$ and 3.2 ± 0.6 eV. Results from the first-principles calculations predict an interstitialcy mechanism for the Zn diffusion when it is not in its trapped state. Using the nudged elastic band method, we obtain a barrier of 1.6 eV for migration of Zn split interstitials (Zn$_i$) in both the [001] and [$\bar{2}$01] directions, in accordance with the results obtained from the trap-limited diffusion model. Interestingly, the Ga vacancy is found to be able to trap two Zn atoms forming a shallow donor complex labeled Zn$_i$Zn$_{Ga}$. The energy needed for Zn$_i$ to dissociate from this donor complex is estimated to be 2.99 eV, in reasonable agreement with the trap dissociation energies extracted from the diffusion model.

I. INTRODUCTION

The large band-gap (4.7–4.9 eV) [1–3], high breakdown field ($\sim$8 MV/cm) [1], high electron mobility (200 cm^2 V^{-1} s^{-1}) [4] and the availability of melt-grown β-Ga$_2$O$_3$ are the key properties making β-Ga$_2$O$_3$ highly a interesting material. As a consequence of these properties, β-Ga$_2$O$_3$ has the potential to be a contender for providing power electronic devices that are smaller, faster and with reduced energy loss compared to current Si-based devices. β-Ga$_2$O$_3$ belongs to a class of materials, which is on one hand, relatively straightforward to dope *n* type. Si and Sn are typically used as donors and yield high electron concentration, whereas also retaining relatively high electron mobility [5–8]. On the other hand, due to self-trapped hole formation and low valence-band dispersion, β-Ga$_2$O$_3$ is challenging to dope *p* type [9,10].

Acceptor levels in β-Ga$_2$O$_3$ are generally deep and can, therefore, mainly be used to compensate *n*type Ga$_2$O$_3$, e.g., for making a semi-insulating layer that can be used in unipolar devices [11]. Mg, Fe, and Zn are some of the acceptors that have been explored for this purpose [12–15]. In order to provide well-controlled doping and long term stability for such devices, it is essential to understand and control the diffusion behavior of these acceptors in β-Ga$_2$O$_3$.

Peelaers *et al.* investigated the diffusion of the Mg impurity using first-principles calculations [13]. This paper showed that it is energetically favorable for Mg$_i$ to share a lattice site with Ga in a mobile split interstitial configuration. Furthermore, it was predicted that the Mg split interstitial can dissociate into Mg$_{Ga}$ and a Ga-split interstitial, where Mg$_{Ga}$ is immobile and considered trapped. Mg can dissociate from the trap upon an encounter with Ga$_i$, and the diffusion of Mg was predicted to be mediated by Ga$_i$. In a Mg diffusion study by Mauze *et al.*

they observed significant redistribution of Mg after annealing in the temperature range 925–1050 °C [16]. They also suggest a rich point defect interaction taking part in the diffusion of Mg.

Fe diffusion in Si-ion-implanted β-Ga$_2$O$_3$ has been studied by Wong *et al.* [17]. It was found that the Fe diffusion is enhanced in Si-implanted regions due to formation of intrinsic defects. However, no diffusion mechanism was suggested. This shows the need for further in-depth studies of Mg, Fe, and Zn diffusions in β-Ga$_2$O$_3$ [16].

In this paper, we have combined first-principles defect calculations with diffusion modeling to describe the concentration vs depth of Zn diffusion in β-Ga$_2$O$_3$ as measured by secondary ion mass spectrometry (SIMS). Zn was systematically introduced into β-Ga$_2$O$_3$ by exposing the samples to vaporized Zn in a sealed quartz ampule. Diffusion profiles were successfully simulated by employing a trap-limited diffusion model (TLD). Based on comparison between the extracted TLD model parameters with values obtained from first-principles calculations, we propose a physical model for the diffusion of Zn in β-Ga$_2$O$_3$.

II. METHODS

A. Experimental details

Single side polished single-crystalline β-Ga$_2$O$_3$ with (001) and ($\bar{2}$01) surface orientations, both grown by the edge defined film-fed growth method (Tamura Corporation, Japan), have been studied. The (001)-oriented samples consisted of an 8-μm layer of β-Ga$_2$O$_3$ grown by halide vapor-phase epitaxy on a Sn-doped β-Ga$_2$O$_3$ substrate whereas the ($\bar{2}$01)-oriented samples were unintentionally doped bulk. The main impurity

in the epitaxial layer was Si ($\sim 10^{16}$ cm^{-3}), whereas the substrate contained Si and Fe ($\sim 10^{17}$ cm^{-3}) in addition to Sn. The full-width at half maximum (FWHM) from x-ray diffraction rocking curve scans was provided by the manufacturer and the details can be found in the Appendix.

To introduce Zn, 5×5 mm^2 pieces of β-Ga$_2$O$_3$ with orientations (001) or ($\bar{2}$01) were put in sealed quartz ampules together with $\sim$0.1-g pieces of 99.98% pure Zn. The quartz ampules were narrowed in the middle keeping the two materials separated, and the ampules were pumped with a rough vacuum before being sealed. The samples were heated to temperatures from 900 to 1100 °C for 1 h. A Cameca IMS7f with a 10-keV O$_2^+$ primary beam raster scanned in an area of 150×150 um^2, was used to obtain concentration vs depth profiles of Zn. To calibrate the depth, the craters were measured with a Dektak 8 stylus profilometer, and a constant sputter rate was assumed. ^{64}Zn-implanted β-Ga$_2$O$_3$ reference samples were used to calibrate the concentration. On a sample previously heated to 1100 °C for 1 h, a second heat treatment was conducted at 1100 °C for 1 h in oxygen flow after removing the Zn source on the sample surface. The sample was then measured using SIMS, and we attempted to measure the sample resistivity with a four-point probe.

B. Computational details

To help identify the prevailing mechanism for Zn diffusion, formation energies and migration barriers of Zn-related and intrinsic defects in β-Ga$_2$O$_3$ were calculated within the framework of the generalized Kohn-Sham theory. We used projector augmented-wave potentials [18,19] as implemented in the VASP code [20] with semicore Ga $3d$ electrons included explicitly as valence electrons.

Unless specified, all calculations were performed using the Heyd-Scuzeria-Ernzerhof (HSE) [21] screened hybrid functional with the fraction of screened Hartree-Fock exchange adjusted to 33%. The bulk lattice constants and internal ionic coordinates of β-Ga$_2$O$_3$ were optimized until the forces were reduced to less than 5 meV/Å, using a plane-wave energy cutoff of 520 eV and a Γ-centered k-point mesh of $8 \times 8 \times 4$. This results in a direct band-gap value of 4.9 eV and lattice parameters $a = 12.23$, $b = 3.03$, $c = 5.79$ Å, and $\beta = 103.8°$, in close agreement with experimental data [22,23].

Defects were modeled in 160-atom supercells ($1 \times 2 \times 4$ repetition of the conventional unit cell) with the lattice parameters fixed to the calculated values above. Ionic relaxation of the defects was performed until forces were smaller than 30 meV/Å, using a plane-wave energy cutoff of 400 eV and a single special k-point at (0.25, 0.25, and 0.25). Formation energies and thermodynamic charge-state transition levels were evaluated using the formalism detailed in Ref. [24]. For example, the formation energy of Zn_{Ga}^q is given by

$$E^f\left(Zn_{Ga}^q\right) = E_{tot}\left(Zn_{Ga}^q\right) - E_{tot}^{bulk} + \mu_{Ga} - \mu_{Zn} + qE_F, \quad (1)$$

where $E_{tot}(Zn_{Ga}^q)$ and E_{tot}^{bulk} are the total energies of the supercell containing Zn_{Ga}^q in charge state q and the bulk crystal, respectively. The additional Zn and removed Ga atoms are exchanged with reservoirs with chemical potentials μ_{Zn} and μ_{Ga}, respectively. The host chemical potentials μ_{Ga} and μ_O are governed by the thermodynamic sta-

bility condition $2\Delta\mu_{Ga} + 3\Delta\mu_O = \Delta H_f(\beta\text{-Ga}_2\text{O}_3)$, where $\Delta H_f(\beta\text{-Ga}_2\text{O}_3) = -10.22$ eV is the calculated heat of formation of β-Ga$_2$O$_3$. The chemical potentials are referenced to the calculated energy per atom in bulk metal Ga and molecular O, corresponding to Ga- and O-rich limits, respectively. Similarly, μ_{Zn} is bound by the stability of the solubility-limiting phase ZnGa$_2$O$_4$. For charged defects, electrons are exchanged with the Fermi level E_F, which is given relative to the valence-band maximum, and a finite-size correction to the formation energy is included by following the scheme outlined in Refs. [25,26].

Defect migration barriers were calculated using the climbing-image nudged elastic band (CI-NEB) method [27], including, at least, five images between the end-point structures. Forces were converged to within 30 meV/Å. Due to the high computational cost associated with hybrid functional CI-NEB calculations, initial CI-NEB calculations were performed using the strongly constrained and appropriately normed (SCAN) [28] semilocal functional. The overall pathway and barrier for migration along each crystal direction was determined based on these initial SCAN results as shown in the Appendix. Next, CI-NEB calculations at the HSE level were performed only for the barrier-limiting diffusion in each crystal direction, using the geometries obtained from the SCAN calculations as a starting point. Only the migration barriers obtained using HSE are discussed in the following. Differences between the migration barriers obtained using SCAN, and HSE results can be found in the Appendix and are on the order of 0.1 eV. Similar differences have been reported for Ga$_i^+$ and V$_{Ga}$ in β-Ga$_2$O$_2$ [29]. The differential equations used to simulate the concentration profiles were solved using the FLEXPDE software [30].

III. RESULTS AND DISCUSSION

Results from SIMS measurements on samples heat treated at temperatures from 900 to 1100 °C are plotted in Fig. 1, where (a) and (b) show Zn diffusion in (001) and ($\bar{2}$01) oriented β-Ga$_2$O$_2$, respectively. In all profiles, we see a concentration of Zn in the range of $(1–5) \times 10^{20}$ cm^{-3} that keeps a close to constant concentration before an abrupt decrease results in a shape resembling that of a box profile. Higher annealing temperatures result in Zn diffusion deeper into the samples and a less sharp profile edge, which is a typical indication of a TLD process [31]. Indeed, a diffusion process limited by trapping of Zn can explain the shape of the profiles. In the TLD model, the time dependence of the concentration of the diffusing specie [Zn] is given as

$$\frac{\partial[Zn]}{\partial t} = D\frac{\partial^2[Zn]}{\partial x^2} - \frac{\partial[Zn_a]}{\partial t}, \quad (2)$$

where D is the diffusivity and $[Zn_a]$ is the concentration of trapped Zn. The concentration of trapped Zn will change as a function of the trapping rate and dissociation rate as follows:

$$\frac{\partial[Zn_a]}{\partial t} = K[Zn][a] - \nu[Zn_a], \quad (3)$$

where $[a]$ is the trap concentration, ν is the dissociation rate, and $K = 2\pi RD$ is the trapping rate with the capture radius R. The model itself does not reveal the identity of the trap.
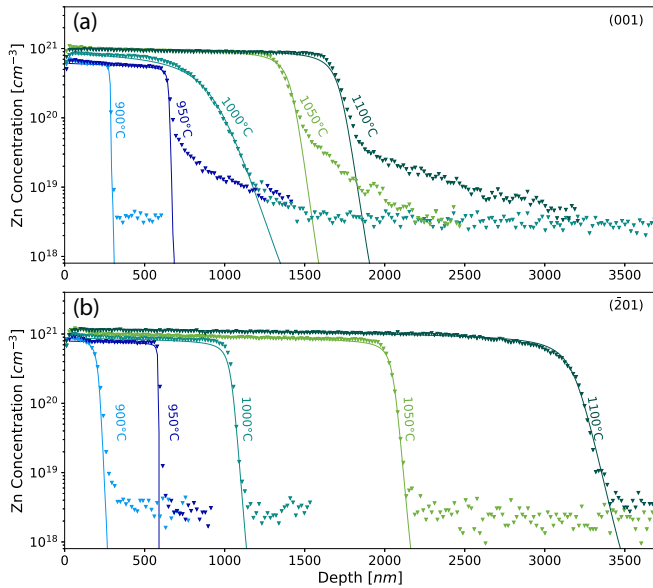
FIG. 1. (a) Zn concentration as a function of depth in (001) and (b) ($\bar{2}$01) β-Ga$_2$O$_3$ for samples heat treated in ampules at 900–1100 °C for 1 h. Dotted lines are data obtained with SIMS, whereas solid lines are simulated with a TLD model. For (001) orientation the concentration of Zn keeps a steady level before there is an abrupt decrease except from the profile with annealing temperature at 1000 °C. The Zn profiles in [$\bar{2}$01] direction has similar shapes as seen in the [001] direction, but diffuses further into the material at temperatures 1050 and 1100 °C.

The simulated profiles can be seen as solid lines in Fig. 1. The capture radius was set to 30 Å [32], whereas the parameters D, ν, and trap concentration were varied to optimize the fits. Fitting parameters can be found in the Appendix. Furthermore, the solubility of interstitial Zn in β-Ga$_2$O$_3$ is defined as a boundary condition at the sample surface. Figure 2 shows
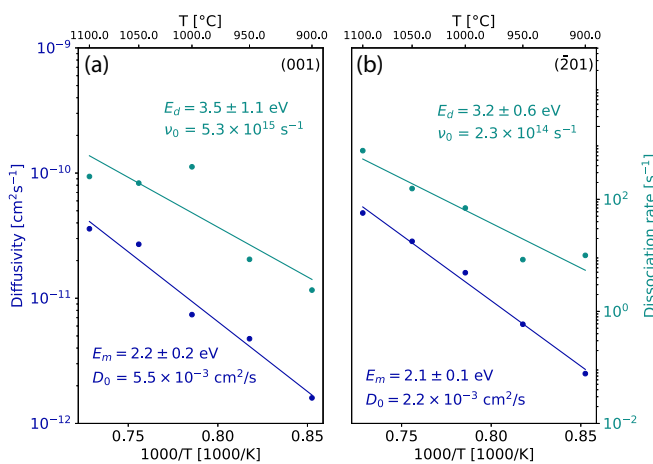

FIG. 2. Diffusivity and dissociation rate as a function of $1000/T$ for concentration profiles measured in (a) [001] and (b) [$\bar{2}$01] directions. The slope of the fitted curves give migrations barriers of $E_m = 2.2 \pm 0.2$ and 2.1 ± 0.1 eV and dissociation energies of $E_d = 3.5 \pm 1.1$ and 3.2 ± 0.6 eV for directions [001] and [$\bar{2}$01], respectively.
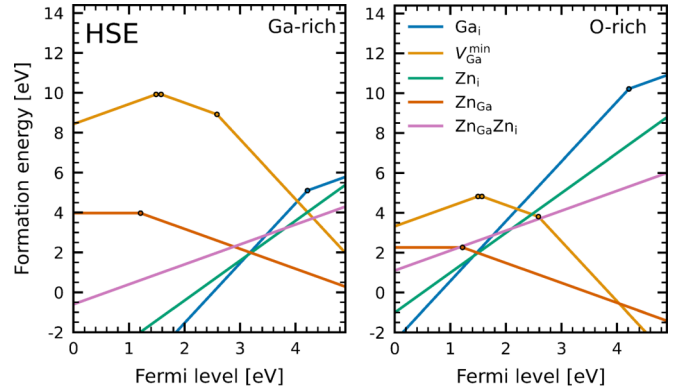

FIG. 3. The calculated formation energies for defects in β-Ga$_2$O$_3$ as a function of Fermi level for Ga-rich (left) and O-rich (right) conditions. Only the lowest-energy configuration under n-type conditions is shown for each defect. The lowest-energy configuration for Zn in n-type β-Ga$_2$O$_3$ is Zn occupying a Ga site.

Arrhenius plots for the diffusivities and dissociation rates extracted from the TLD modeling, where (a) and (b) correspond to (001) and ($\bar{2}$01) orientations, respectively. From the temperature dependence of the diffusivity and dissociation rate, the slopes of the Arrhenius plots result in migration barriers of $E_m = 2.2 \pm 0.2$ and 2.1 ± 0.1 eV and dissociation energies of $E_d = 3.5 \pm 1.1$ and 3.2 ± 0.6 eV for orientations (001) and ($\bar{2}$01), respectively. We see a notable difference between the two directions in the diffusion length at temperatures 1050 and 1100 °C. The migration barrier in the two directions is similar both from experimental and from calculated values and will be discussed later. However, there might be differences in the diffusion pathway causing the different diffusion length in the two directions. Further investigation is required to confirm the cause for the different diffusion lengths. It is important to note that during the SIMS measurements, we observed no indication of charging effects, indicating that the samples were still conductive after heat treatment in Zn atmosphere in the sealed evacuated quarts ampules.

One sample was heat treated a second time in oxygen flow at 1100 °C. In this sample, we observed strong charging during the SIMS measurement. Moreover, we were not able to measure the sample by four-point probe, strongly indicating that the sample resistivity was high.

The formation energies for Ga$_i$, V$_{Ga}$, Zn$_i$, Zn$_{Ga}$ and Zn$_{Ga}$Zn$_i$ in β-Ga$_2$O$_3$ obtained from hybrid-functional calculations are shown in Fig. 3 for both Ga-rich and O-rich conditions. Since no charging was observed in the SIMS measurements, indicating conductive samples, we look at n-type conditions to explain the diffusion mechanism. For n-type conditions, the most stable defect configuration is Zn$_{Ga}$. Zn and Ga in a split interstitial configuration on a Ga site (Zn$_i$) is the second most favorable configuration. Figure 4 shows the relaxed structure for all atomic configurations of the Zn interstitial (Zn$_i$) found in the present paper. The Ga sites (Ga1 and Ga2), O sites (O1–O3) and interstitial sites (ia, ib, ic, id, ie, and if) are labeled in accordance with previous works [33–36].

Similar to Mg$_i$ in β-Ga$_2$O$_3$ [13], we find that Zn$_i$ prefers to form a split-interstitial configuration in which one Zn ion
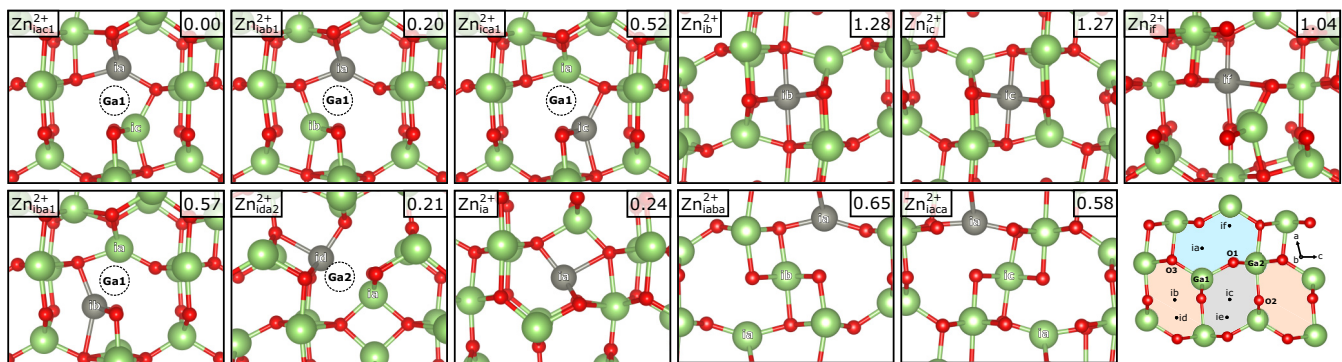
FIG. 4. Relaxed structures of eleven different Zn_i configurations in the 2+ charge state. The energy relative to the lowest-energy Zn_{iac1} is indicated for each structure, given in units of eV. The monoclinic β-Ga_2O_3 structure is shown in the bottom right corner with the Ga, O, and interstitial sites and different channels indicated. All structures are viewed along the [010] direction.

and one Ga ion share a single Ga site. The relative energies of different configurations are indicated in Fig. 4. The most energetically favorable configuration is a split interstitial on the Ga1 site with the Zn and Ga ions displaced towards the ia and ic sites, respectively, which we denote here as Zn_{iac1}. The Zn-split interstitial on a Ga2 site is 0.2 eV higher in energy and is only stable in the configuration with Zn and Ga residing near the id and ia sites, respectively (Zn_{ida2}). The other permutation, i.e., with Zn near the ia site and Ga near the id site (Zn_{iad2}), relaxes into the Zn_{ia} regular-interstitial configuration. The Zn interstitial strongly prefers fourfold coordination. Indeed, the regular-interstitial configurations with Zn residing in octahedral interstitial sites ib, ic, or if are 1.0–1.3 eV higher in energy relative to the Zn_{iac1} configuration.

If one were to consider a vacancy-mediated mechanism, one would need to bear in mind that both Zn_{Ga} and V_{Ga} are acceptors and would, therefore, repel each other. Moreover, the formation of Zn_{Ga} would according to Fig. 3 lead to a lowering of the Fermi-level position and, thus, a strong increase in the formation energy of V_{Ga}. Both effects would independently severely limit the effective diffusion of Zn. Thus, we can safely rule out any significant contribution from vacancy -mediated diffusion of Zn. Moreover, considering the high formation energy of Ga_i under n-type conditions, a substitutional-interstitial mechanism in which Zn_{Ga} is converted to mobile Zn_i in the presence of Ga_i is ruled out. This mechanism is more likely to play a role in compensated material as suggested previously for Mg diffusion by Peelaers *et al.* [13]. The focus in the following will, therefore, be on interstitialcy mediated diffusion of Zn limited by the presence of a trap.

Table I lists the migration barriers (E_m) of Zn_i^{2+}, Ga_i^{3+} and Ga_i^{1+} in different crystal directions, as obtained from hybrid-functional calculations. The values for Ga_i are taken from Ref. [29]. A detailed description of the overall pathways for Zn_2^+ migration in different crystal directions can be found in the Appendix. The split interstitial Zn_i is expected to be a mobile species at the experimentally investigated temperature range with a migration barrier of $E_m = 1.62$ eV in the directions [001] and [100], and 0.71 eV in the [010] direction. Diffusion along [$\bar{2}$01] has equal components from the [100] and [001] paths and is expected to have a simi-

lar migration barrier as the [001] and [100] directions. The calculated migration barrier for Zn_i of 1.62 eV is somewhat lower than the migration barriers found from the trap limited diffusion model, i.e., $E_m = 2.2$ eV for [001] and $E_m = 2.1$ eV [$\bar{2}$01]. However, the prediction of an equal overall migration barrier for the [100] and [001] directions is consistent with the extracted migration barriers being similar for the two orientations.

There are, at least, two possibilities to go from the mobile split-interstitial configuration to a highly stable Zn configuration: (i) Zn_i can encounter and fill a V_{Ga}, resulting in Zn_{Ga}, or (ii) dissociation of the Zn split interstitial, resulting in Zn_{Ga} and a Ga split interstitial,

$$(i) \quad Zn_i + V_{Ga} \rightarrow Zn_{Ga}$$

$$(ii) \quad Zn_i + Ga_{Ga} \rightarrow Zn_{Ga} + Ga_i. \quad (4)$$
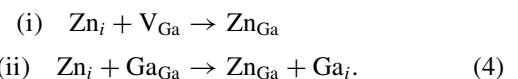
Reaction (ii) is associated with an energy cost of 0.69 eV when the Fermi level is at the conduction-band edge (calculated as the difference between the formation energy of Zn_i and the sum of the formation energies of Zn_{Ga} and Ga_i) as shown in Table II. A low dissociation energy of 1.61 eV can then be obtained by adding the 0.92 eV migration barrier of Ga_i^+ to the binding energy of the split interstitial Zn_i 0.69 eV. Thus, under the relevant experimental conditions, Ga_i should be able to dissociate from Zn_i and diffuse away from the resulting Zn_{Ga}. At this point, it could be tempting to conclude that the diffusion process is fully described by Zn alternating between the mobile split interstitial configuration and a trapped configuration with the Zn at a Ga site.

As shown in Table II the binding energy for Zn_{Ga} is 7.08 eV. When the dissociation energy is estimated as the sum

TABLE I. Calculated migration barriers (E_m) for split interstitial Zn (Zn_i) and Ga_i for three directions in β-Ga_2O_3 .

Specie	E_m (eV)		
	[100]	[010]	[001]
Zn_i^{2+}	1.62	0.71	1.62
Ga_i^{3+}	1.02	0.72	0.80
Ga_i^+	2.16	0.92	2.16

TABLE II. Calculated binding energies (E_b) for complexes in [001] and [100] directions when the Fermi-level is at the CBM.

Complex	E_b (eV)
$Zn_i \rightarrow Zn_{Ga} + Ga_i$	0.69
$Zn_{Ga} \rightarrow V_{Ga} + Zn_i$	7.08
$Zn_{Ga}Zn_i \rightarrow Zn_{Ga} + Zn_i$	1.37

of the binding energy and the migration barrier for the mobile point defect, i.e., 1.62 eV for the split interstitial Zn, it results in a dissociation energy of 8.70 eV. This energy is so high that for any relevant conditions Zn will not dissociate from V_{Ga} into the interstitial configuration once trapped. In contrast, we clearly observe dissociation from the trap in the SIMS profiles and extracted a dissociation barrier of about 3.2–3.5 eV from the TLD model. This indicates that the observed dissociation does not describe the dissociation of Zn from a Ga vacancy but must have a different origin.

Interestingly, the formation energies in Fig. 3 reveal that Zn_{Ga} can also act as a trap for a second Zn, resulting in a doubly filled Ga vacancy ($Zn_{Ga}Zn_i$). This complex acts as a donor and has a binding energy of about 1.4 eV and, thus, a dissociation energy of about 3.0 eV, which is only slightly lower than the extracted value of 3.2/3.5 eV from the TLD model.

After the first heat treatment in Zn atmosphere, the model suggests that the samples were dominated by $Zn_{Ga}Zn_i$ donors and were, therefore, conductive, consistent with our observations. Note that it was not possible to extract the conductivity of the layer, from, e.g., Hall effect measurements due to the conductive substrate. After the second heat treatment in oxygen flow, the $Zn_{Ga}Zn_i$ donors should according to our theoretical results dissociate and leave the stable Zn_{Ga} acceptors behind. Zn_i may diffuse through the split interstitial configuration, and dissociate into Zn_{Ga} and Ga_i. The highly mobile Ga_i will at the elevated temperature in oxygen flow diffuse to the surface or into the bulk and result in a highly resistive Zn-rich region dominated by the Zn_{Ga} acceptors. Indeed, Zn acting as acceptors in β-Ga_2O_3 is consistent with our experimental observations and in line with that reported by Gustafson *et al.* (in this case the resistivity of the layer was beyond what could be measured using our Hall effect system) [37].

All profiles measured with SIMS exhibit an abrupt drop in concentration from a steady level and has the shape of box profiles, see Fig. 1, except the profiles measured on (001) β-Ga_2O_3 at 1000 °C and ($\bar{2}$01) β-Ga_2O_3 at 900 °C. The diffusivity found from fitting the profile at 1000 °C fits into the Arrhenius relation with the other profiles in the [001] direction. However, the dissociation energy does not fit with what we expect regarding the dissociation rate of the other profiles in the [001] direction. However, SIMS revealed a somewhat higher concentration of Al in the specific sample with the higher dissociation rate as compared to the other samples, potentially due to variation in the as-grown material. The Al doses that were measured in the diffusion regions in the samples have been included in Table IV in the Appendix. A similar effect was also seen for other samples from the same wafer (not shown). We may, therefore, speculate that Al on the Ga site (Al_{Ga}), might act as a trap for a Zn_i forming a

$Al_{Ga}Zn_i$ complex with a higher dissociation rate. However, the calculated binding energy between Al_{Ga} and Zn_i is negligible compared to that of Zn_{Ga} and Zn_i. The most probable source of Al in our samples is Al impurities in the 99.98% pure metallic Zn source. However, additional experiments would be necessary, which is beyond the scope of the current paper.

It should also be noted that the rather high concentration of Zn of $\sim 10^{20}$ cm^{-3} as measured in the samples, is then the sum of all the three main configurations of Zn ($Zn_{Ga}Zn_i$ donors, Zn_{Ga} acceptors, and Zn_i donors).

IV. CONCLUSION

In conclusion, we have found that Zn diffuses through a split interstitial mechanism and is limited by trapping through the formation of a Zn_iZn_{Ga}-donor complex. The donor complex can dissociate into the acceptor state Zn_{Ga} and the mobile donor state Zn_i. Further dissociation of Zn_{Ga} is effectively prevented by a high binding energy 7.08 eV. The combined formation of both donor and acceptor configurations of Zn explain the surprisingly high concentration of Zn introduced into the β-Ga_2O_3 during the Zn diffusion. Furthermore, it is of general interest, that we predict and indirectly observe the ability to fill a Ga vacancy with two Zn atoms, indicating that this might also be the case for similar acceptor impurities, such as Mg in β-Ga_2O_3.

APPENDIX

A. Zn interstitial migration pathways and energy barriers

In the main article, we listed the migration barriers of Zn_i^{2+} for each crystal direction as obtained from hybrid-functional NEB calculations. These calculations were started from geometries obtained from exploratory SCAN NEB calculations. Here, we describe the overall pathways obtained from these SCAN calculations in more detail and compare the overall migration barriers obtained from SCAN and HSE calculations. The results for Zn_i^{2+} and Ga_i^{3+} are also compared. Figure 5 shows the potential-energy profiles obtained from SCAN NEB calculations for the pathways yielding the lowest overall barriers for Zn_{iac1}^{2+} (the lowest-energy atomic configuration of Zn_i^{2+}) to move into an equivalent adjacent site in the three different crystal directions. The pathways are also described using relaxed structures from the NEB calculations.

The lowest overall migration barrier is 0.71 eV (0.54 eV when SCAN is employed) and is found for the [010] direction where Zn migrates within the large eight-sided channel. Among the different mechanisms that were explored, the one with the lowest-energy barrier consists of two jumps: (i) Transformation from the Zn_{iac1}^{2+} split-interstitial configuration to the Zn_{ia}^{2+} regular interstitial configuration, and (ii) Migration along [010] by jumping to the nearest *ia* site. Note that
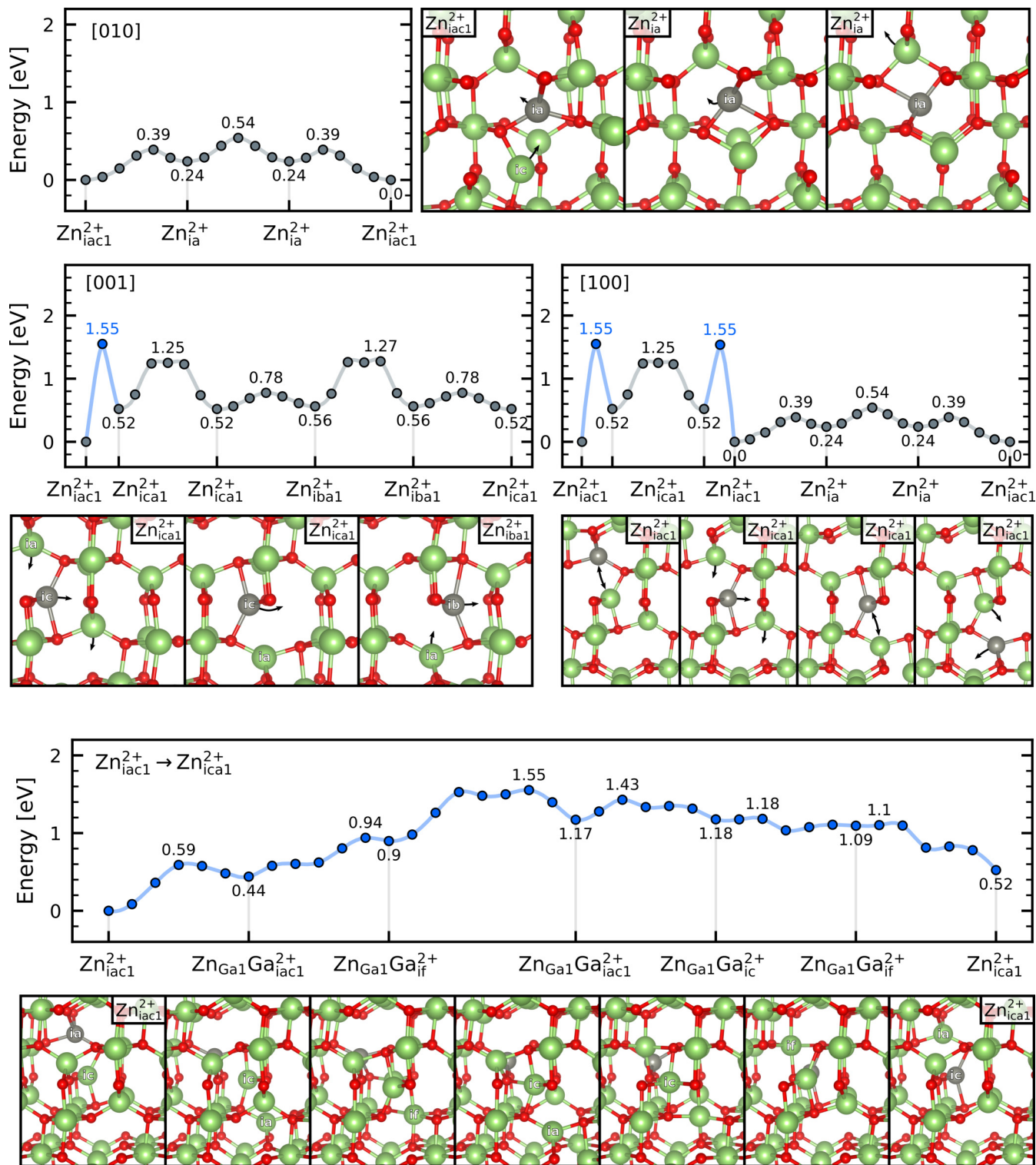
FIG. 5. Overall barriers for Zn_{iac1}^{2+} migration along each crystal direction as obtained from NEB calculations employing the SCAN functional. Structures with arrows describing the migration pathways are shown next to each plot. For migration along the [100] direction, the three final steps are equivalent to those shown for migration along [010]. The bottom plot (blue) and structures show the pathway with the lowest overall barrier of 1.55 eV for the Zn and Ga ions to swap positions in Zn_{iac1}^{2+} (resulting in Zn_{ica1}^{2+}). This path is reduced to a single point for [001] and [100].

Zn_{ia}^{2+} is located somewhat off the ideal *ia* site, near the center of the large eight-sided channel as shown in Fig. 4. Ga_i^{3+} also prefers the Ga_{iac1}^{3+} configuration, but Ga_{ia}^{3+} is unstable, and

migration along the [010] direction rather proceeds via Ga_{if}^{3+}. Even so, the calculated Ga_i^{3+} migration barrier of 0.72 eV is close to the 0.71 eV found for Zn_i^{2+}.

TABLE III. The parameters used to obtain the best fit to the measured concentration profiles.

Parameter	900 °C	950 °C	1000 °C	1050 °C	1100 °C
Number of traps (001) *(cm^{-3})	6.30×10^{20}	5.50×10^{20}	8.75×10^{20}	9.39×10^{20}	9.39×10^{20}
Number of traps ($\bar{2}$01) (cm^{-3})	9.10×10^{20}	7.40×10^{20}	8.20×10^{20}	8.35×10^{20}	9.50×10^{20}
Solid solubility (001) (cm^{-3})	4.00×10^{19}	6.50×10^{19}	9.10×10^{19}	8.40×10^{20}	9.60×10^{20}
Solid solubility ($\bar{2}$01) (cm^{-3})	1.55×10^{19}	5.45×10^{19}	6.90×10^{19}	1.68×10^{20}	2.70×10^{20}
ν (001) (s^{-1})	2.4	8.5	380.9	195	255.9
ν ($\bar{2}$01) (s^{-1})	10	8.4	70	155.9	740
D (001) (cm^2 s^{-1})	$1.6e \times 10^{-12}$	$4.75e \times 10^{-12}$	$7.4e \times 10^{-12}$	$2.7e \times 12^{-11}$	$3.59e \times 10^{-11}$
D ($\bar{2}$01) (cm^2 s^{-1})	$2.5e \times 10^{-12}$	$6.2e \times 10^{-12}$	$1.6e \times 10^{-11}$	$2.85e \times 10^{-11}$	$4.8e \times 10^{-11}$

For the remaining two directions, we obtain a significantly larger Zn_i^{2+} migration barrier of 1.61 eV (1.55 eV when SCAN us used). For comparison, the maximum migration barrier predicted for Ga_i^{3+} is only 1.02 eV (for the [100] direction). The main reason for this difference is the fact that the Zn and Ga ions have two permutations for each split-interstitial configuration. For Ga_{iac1}^{3+} migration, it does not matter which of the two Ga ions comprising the split-interstitial makes the jump (the other becoming Ga1 substitutional). Thus, the Ga ion located near the ia site can easily migrate along [010] within the eight-sided channel, or the other Ga ion located near the ic site can migrate along [001] by jumping between ic and ib sites in neighboring irregular-hexagon channels. For Zn_{iac1}^{2+}, however, the Zn ion resides near the ia site. In order for Zn_{iac1}^{2+} to migrate along [001] or [100], the Zn ion has to enter/cross the irregular-hexagon channel. We find that this is not as easily accomplished for Zn_{iac1}^{2+} (compared to Ga_{iac1}^{3+}) because the Ga ion located near the ic site blocks the most direct route for the Zn ion to enter the irregular-hexagon channel; if the Zn and Ga ions in Zn_{iac1}^{2+} could swap positions, migration along the [001] and [100] directions would be facile.

We have considered two different mechanisms by which the Zn ion in the Zn_{iac1}^{2+} split-interstitial can enter the irregular-hexagon channel: (i) Transformation from Zn_{iac1}^{2+} to Zn_{ia}^{2+} (equivalent to the first step for Zn_i^{2+} migration along the [010] direction), followed by a Zn jump into the nearest irregular-hexagon channel to form Zn_{ica1}^{2+}. This mechanism provides the shortest route (two jumps), but the second jump results in a high overall barrier of 2.27 eV (2.27 eV when SCAN is used) (not shown). (ii) Partial dissociation of Zn_{iac1}^{2+} to form Zn_{Ga1}^- and Ga_{iac1}^{3+} at adjacent Ga1 sites (can be viewed as a $(Zn_{Ga1}Ga_{iac1})^{2+}$ complex), followed by reformation of the Zn split interstitial in the Zn_{ica1}^{2+} arrangement. Here, the Zn ion remains on the Ga1 site and Ga ions move around. We find that a route within the second mechanism yields the lowest overall barrier of 1.61 eV, but consists of a large number of jumps, as shown in Fig. 5. The 1.61-eV overall barrier for the Zn and Ga ions in Zn_{ica1}^{2+} to swap positions (resulting in Zn_{iac1}^{2+})

represents the bottleneck for migration in both the [100] and [001] directions. For the [100] direction, the remaining path after crossing the irregular-hexagon channel is equivalent to the one for [010] in Fig. 5. For the [001] direction, once the Zn and Ga ions have swapped positions, the Zn ion can migrate easily between ic and ib sites along [001]. Thus, the overall [100] and [001] migration barriers are limited by the same 1.61 eV barrier for Zn and Ga to swap positions, but migration along [001] requires significantly fewer steps.

B. Experimental details

Novel Crystal Technology Inc. provided data sheets with measured material parameters including parameters on the crystal quality from x-ray diffraction. According to the wafer data sheet the (001) oriented β-Ga$_2$O$_3$ wafer has an offset of $0.0°$ and $0.1°$ toward the [100] and [010] directions, respectively, whereas the ($\bar{2}$01) has an offset of $0.0°$ and $0.7°$ in the [010] and [102], respectively. In addition, the FWHM of the (001) reflection is 23 and 27 arcsec in the [100] and [010] azimuthal directions, respectively, for (010) orientation and 15 and 25 arcsec in the [010] and [102] azimuthal directions, respectively for the ($\bar{2}$01) orientation.

C. Fitting parameters in the diffusion simulations

Table III shows the fitting parameters used in FLEXPDE to simulate the concentration profiles where D is the diffusivity and ν is the dissociation rate. The length of the system L was set to 20×10^{-4} cm. L is set long enough that the boundary conditions furthest away from the surface will not effect the diffusion simulations. The number of traps was set to the highest concentration which coincide with the concentration plateau of the trap limited diffusion profiles.

D. Impurity doses

Al doses in the samples obtained from SIMS measurements can be found in Table IV.

TABLE IV. Al doses in all samples obtained from integrating the SIMS profiles in the diffusion regions.

	900 °C	950 °C	1000 °C	1050 °C	1100 °C
Al dose (001) (cm^{-2})	1.99×10^{12}	3.08×10^{12}	1.79×10^{13}	3.22×10^{12}	1.26×10^{12}
Al dose ($\bar{2}$01) (cm^{-2})	1.23×10^{14}	4.11×10^{11}	5.02×10^{12}	2.01×10^{12}	3.57×10^{12}

[1] M. Higashiwaki, K. Sasaki, A. Kuramata, T. Masui, and S. Yamakoshi, Phys. Status Solidi A **211**, 21 (2014).

[2] M. Orita, H. Ohta, M. Hirano, and H. Hosono, Appl. Phys. Lett. **77**, 4166 (2000).

[3] H. H. Tippins, Phys. Rev. **140**, A316 (1965).

[4] N. Ma, N. Tanen, A. Verma, Z. Guo, T. Luo, H. G. Xing, and D. Jena, Appl. Phys. Lett. **109**, 212101 (2016).

[5] Z. Feng, A. F. M. Anhar Uddin Bhuiyan, M. R. Karim, and H. Zhao, Appl. Phys. Lett. **114**, 250601 (2019).

[6] K. Goto, K. Konishi, H. Murakami, Y. Kumagai, B. Monemar, M. Higashiwaki, A. Kuramata, and S. Yamakoshi, Thin Solid Films **666**, 182 (2018).

[7] K. Sasaki, M. Higashiwaki, A. Kuramata, T. Masui, and S. Yamakoshi, J. Cryst. Growth **392**, 30 (2014).

[8] S.-H. Han, A. Mauze, E. Ahmadi, T. Mates, Y. Oshima, and J. S. Speck, Semicond. Sci. Technol. **33**, 045001 (2018).

[9] H. Peelaers and C. G. Van de Walle, Phys. Status Solidi B **252**, 828 (2015).

[10] J. Varley, A. Janotti, C. Franchini, and C. Van De Walle, Phys. Rev. B **85**, 081109(R) (2012).

[11] M. Higashiwaki and S. Fujita, *Gallium Oxide*, Springer Series in Materials Science (Springer, Cham, 2020), Vol. 293.

[12] A. T. Neal, S. Mou, S. Rafique, H. Zhao, E. Ahmadi, J. S. Speck, K. T. Stevens, J. D. Blevins, D. B. Thomson, N. Moser, K. D. Chabak, and G. H. Jessen, Appl. Phys. Lett. **113**, 062101 (2018).

[13] H. Peelaers, J. L. Lyons, J. B. Varley, and C. G. Van de Walle, APL Mater. **7**, 022519 (2019).

[14] J. L. Lyons, Semicond. Sci. Technol. **33**, 05LT02 (2018).

[15] E. Chikoidze, T. Tchelidze, C. Sartel, Z. Chi, R. Kabouche, I. Madaci, C. Rubio, H. Mohamed, V. Sallet, F. Medjdoub, A. Perez-Tomas, and Y. Dumont, Mater. Today Phys. **15**, 100263 (2020).

[16] A. Mauze, Y. Zhang, T. Itoh, T. E. Mates, H. Peelaers, C. G. Van de Walle, and J. S. Speck, J. Appl. Phys. **130**, 235301 (2021).

[17] M. H. Wong, K. Sasaki, A. Kuramata, S. Yamakoshi, and M. Higashiwaki, Appl. Phys. Lett. **106**, 032105 (2015).

[18] P. E. Blöchl, Phys. Rev. B **50**, 17953 (1994).

[19] G. Kresse and D. Joubert, Phys. Rev. B **59**, 1758 (1999).

[20] G. Kresse and J. Furthmüller, Phys. Rev. B **54**, 11169 (1996).

[21] A. V. Krukau, O. A. Vydrov, A. F. Izmaylov, and G. E. Scuseria, J. Chem. Phys. **125**, 224106 (2006).

[22] C. Janowitz, V. Scherer, M. Mohamed, A. Krapf, H. Dwelk, R. Manzke, Z. Galazka, R. Uecker, K. Irmscher, R. Fornari, M. Michling, D. Schmeißer, J. R. Weber, J. B. Varley, and C. G. Van de Walle, New J. Phys. **13**, 085014 (2011).

[23] J. Åhman, G. Svensson, and J. Albertsson, Acta Crystallogr. C Struct. Chem. **52**, 1336 (1996).

[24] C. Freysoldt, B. Grabowski, T. Hickel, J. Neugebauer, G. Kresse, A. Janotti, and C. G. Van de Walle, Rev. Mod. Phys. **86**, 253 (2014).

[25] C. Freysoldt, J. Neugebauer, and C. G. Van de Walle, Phys. Rev. Lett. **102**, 016402 (2009).

[26] Y. Kumagai and F. Oba, Phys. Rev. B **89**, 195205 (2014).

[27] G. Henkelman, B. P. Uberuaga, and H. Jansson, J. Chem. Phys. **113**, 9901 (2000).

[28] J. Sun, A. Ruzsinszky, and J. P. Perdew, Phys. Rev. Lett. **115**, 036402 (2015).

[29] Y. K. Frodason, J. B. Varley, K. M. H. Johansen, L. Vines, and C. G. Van de Walle, Phys. Rev. B **107**, 024109 (2023).

[30] PDE Solutions Inc., FLEXPDE (2019).

[31] V. M. Reinertsen, P. M. Weiser, Y. K. Frodason, M. E. Bathen, L. Vines, and K. M. Johansen, Appl. Phys. Lett. **117**, 232106 (2020).

[32] M. S. Janson, A. Hallén, M. K. Linnarsson, and B. G. Svensson, Phys. Rev. B **64**, 195202 (2001).

[33] J. B. Varley, H. Peelaers, A. Janotti, and C. G. Van de Walle, J. Phys.: Condens. Matter **23**, 334212 (2011).

[34] A. Kyrtsos, M. Matsubara, and E. Bellotti, Phys. Rev. B **95**, 245202 (2017).

[35] J. M. Johnson, Z. Chen, J. B. Varley, C. M. Jackson, E. Farzana, Z. Zhang, A. R. Arehart, H.-L. Huang, A. Genc, S. A. Ringel, C. G. Van de Walle, D. A. Muller, and J. Hwang, Phys. Rev. X **9**, 041027 (2019).

[36] Y. K. Frodason, C. Zimmermann, E. F. Verhoeven, P. M. Weiser, L. Vines, and J. B. Varley, Phys. Rev. Mater. **5**, 025402 (2021).

[37] T. D. Gustafson, J. Jesenovec, C. A. Lenyk, N. C. Giles, J. S. McCloy, M. D. McCluskey, and L. E. Halliburton, J. Appl. Phys. **129**, 155701 (2021).